Imaging the Footprint of Nanoscale Electrochemical Reactions for Assessing Synergistic Hydrogen Evolution

Louis Godeffroy, Paolo Ciocci, Nathaly Ortiz Peña, Damien Alloyeau,
Jean-Marc Noël, Jean-françois Lemineur, Frédéric Kanoufi

To cite this version:

Louis Godeffroy, Paolo Ciocci, Nathaly Ortiz Peña, Damien Alloyeau, Jean-Marc Noël, et al.. Imaging the Footprint of Nanoscale Electrochemical Reactions for Assessing Synergistic Hydrogen Evolution. Angewandte Chemie International Edition, 2023, 62 (29), 10.1002/anie.202304950 . hal-04237650

HAL Id: hal-04237650
https://hal.science/hal-04237650v1

Submitted on 11 Oct 2023

Imaging the Footprint of Nanoscale Electrochemical Reactions for Assessing Synergistic Hydrogen Evolution

Louis Godeffroy,[a] Paolo Ciocci,[a] Nathaly Ortiz Peña,[b] Damien Alloyeau,[b] Jean-Marc Noël,[a] Jean-François Lemineur,[a] Frédéric Kanoufi[a],*

[a] L. Godeffroy, Dr P. Ciocci, Dr J.-M. Noël, Dr. J.-F. Lemineur, Dr, F. Kanoufi
Université Paris Cité, CNRS, ITODYS, F-75013 Paris, France
E-mail: frederic.kanoufi@u-paris.fr

[b] Dr. N. Ortiz Peña, Dr. D. Alloyeau
Université Paris Cité, CNRS, Laboratoire Matériaux et Phénomènes Quantiques, F-75013 Paris, France

Supporting information for this article is given via a link at the end of the document.

Abstract: This work proposes a novel method for measuring the intrinsic activity of single metal-based nanoparticles towards water reduction in neutral media at industrially relevant current densities. Instead of using gas nanobubbles as proxy, the method uses optical microscopy to track the local footprint of the reaction through the precipitation of metal hydroxide, which is associated to the local pH increase during electrocatalysis. The results show the electrocatalytic activities of different types of metal nanoparticles and bifunctionnal core-shell nanostructures made of Ni and Pt, and demonstrate the importance of metal hydroxide nano-shells in enhancing electrocatalysis. This method should be generalizable to any electrocatalytic reaction involving pH changes such as nitrate or CO_2 reduction.

Introduction

Water splitting is the cornerstone for various solutions to environmental sustainability, from energy conversion and storage to water purification and desalination. While significant research efforts are being devoted to the environmentally friendly production of molecular hydrogen, based on the hydrogen evolution reaction (HER), they need to be undertaken in concert with the limitations from its counterpart reaction, the oxygen evolution reaction (OER). Indeed, the lower stability of OER catalysts in acidic conditions calls for novel engineering strategies to produce multi-functional electrode materials suitable for HER in neutral or alkaline electrolytes, i.e. following reactions (1-3).[1–3] For instance, the classical Pt-group metals are good catalysts for the recombination of hydrogen intermediates (Tafel step, (2)), but show poor activation for the dissociation of water (Volmer step, (1)). This kinetically limiting initial step in neutral and alkaline conditions makes the overall HER (3) 2 to 3 orders of magnitude slower than in acidic conditions.[4]

$$H_2O + e^- \rightarrow H^* + HO^- \qquad (1)$$

$$2H^* \rightarrow H_2 \qquad (2)$$

$$2H_2O + 2e^- \rightarrow H_2 + 2HO^- \qquad (3)$$

Alternatively, metal oxides or hydroxides, due to their high oxophilicity, promote the HO-H bond dissociation, but are generally poor catalysts for the H^* recombination step (2).

A promising strategy to both accelerate H_2O dissociation and keep a high H^* recombination rate consists in engineering bifunctional materials, as proposed in 2011 by Markovic *et al.*[5] They showed that the addition of $Ni(OH)_2$ clusters on Pt(111) improved the catalytic activity of Pt(111) in 0.1 M KOH by a factor of 8. The catalytic activity could be improved even further (by an overall factor of 10) with the addition of Li^+ in the electrolyte. $Ni(OH)_2$-Pt edges were suggested to facilitate the water dissociation step (1) due to the higher oxophilicity of $Ni(OH)_2$ which adsorbs HO^- more easily than Pt(111), and Li^+ was suggested to weaken the HO-H bond through non-covalent interactions. This discovery led to the development of numerous catalysts featuring large numbers of $Ni(OH)_2$-Pt edges. To further decrease the cost of these catalysts, the amount of Pt was often optimized by using carefully positioned Pt nanostructures.[6–11]

Apart from Pt, Markovic's strategy was also successively applied to Earth-abundant metals such as Ni, Cu and Ag, making such bifunctional catalysts even more cost-effective.[12] In each case, adding $Ni(OH)_2$ clusters on the metal surface enhanced the catalytic activity to the same level as the bare metal surface in acidic electrolyte. This bifunctional HER activity enhancement has since then been transposed to a wider range of materials and interfaces. Despite the effectiveness of this strategy, the mechanistic understanding of the improved catalytic activity is still under discussion. For example, the increased activity of Pt attributed to the oxophilicity of vicinal $Ni(OH)_2$ (or other metal hydroxides[13,14]) could rather be attributed, based on different *operando* strategies to monitor the Pt(111)-$Ni(OH)_2$ interface, to the disturbance of the local electric field by $Ni(OH)_2$ and the reorganization of the water network.[15]

Even if the bifunctional effect was also reported on nano-catalysts,[16] it remains rarely studied at the single nanoparticle (NP) level. Yet studying individual NPs is crucial to understand such bifunctional nano-catalysts as their size, shape, composition and/or surface state might vary from one NP to another unlike single-crystalline surfaces.[17] Employing the nano-impact method to study individual Ni@NiO NPs, Compton *et al.*[18] showed that their electrochemistry is controlled by the surface oxide layer and not by a size effect. However, experiments were carried out at pH 1.95, which is not representative of the literature. Moreover, the effect of oxide coverage was not investigated.

Besides, scanning probe microscopies[19–21] and optical microscopies[22–24] have also been used to probe the catalytic activity of single NPs. Optical microscopies offer a high temporal and spatial resolution at high throughput. They can readily be used *operando* and coupled to other microscopies.[25] However, they are mostly limited to reactions involving gas bubble formation (HER,[23,24,26,27] OER[22,27]) and thus to very active materials (Pt). If gas nanobubbles are pertinent reporters of the electro- or photocatalytic activity of catalysts, their nucleation on a surface requires local oversaturation, which is only reached at extreme current densities. For example, the nucleation of an individual H_2 nanobubble from the reduction of H^+ in acidic electrolytes at a 100 nm nanoelectrode requires roughly 30 nA of current,[28] which is equivalent to a current density of 400 A/cm^2. This kind of current density is only achievable at impractical overpotentials and even so difficult to reach from the reduction of water in neutral electrolytes.

Herein, we propose a novel approach to image and quantify *operando* the catalytic activity of single electrocatalytic NPs (Ni and Pt) towards water reduction, as well as bifunctional NPs made of Ni and Pt NPs coated with a metal hydroxide/oxide nanoshell. As schematized in Figure 1, instead of visualizing the formation of a bubble, the strategy focuses on evaluating the production of H_2 based on the rate of formation of HO^-. Instead of using fluorescence microscopy,[29–33] we propose a reporting strategy using the ability of metal ions, M^{n+}, to precipitate hydroxides, $M(OH)_n$, as a nanometer-thick layer around individual NPs. This precipitation layer is monitored *operando* by refractive index sensitive optical microscopy, interference reflection microscopy. It is detected as a halo expanding around the NP as the electrocatalysis of water reduction proceeds. Supported by finite element simulations, the dynamics of the halo's expansion can be used as a proxy for the electrocatalytic activity of the NPs. This concept is illustrated here in the case of the activity of Ni and Pt NPs in the presence of Ni^{2+} and Mg^{2+}, hence through the production of a $Ni(OH)_2$ and $Mg(OH)_2$ layer, respectively. In turn, it allows inspecting the reactivity of the bifunctional core-shell nanocatalysts $Ni@Ni(OH)_2$, $Pt@Ni(OH)_2$ and $Pt@Mg(OH)_2$, and to compare their performance to that of bare Ni and Pt NPs.

Results and Discussion

The experimental configuration is schematized in Figure 1a (details can be found in the SI, section SI1). A droplet of 1 mM MCl_2 + 0.1 M KCl (M=Ni, Mg) solution is confined between an indium tin oxide (ITO)-coated glass coverslip – which serves as optical sensor – and a glass micropipette (ca. 100 µm in diameter, not shown in Figure 1a) filled with the electrolyte and containing a Pt wire. The whole forms a microelectrochemical cell where the ITO also plays the role of working electrode (WE) and the Pt wire the role of quasi-reference counter electrode (QRCE) in a two-electrode configuration. The ITO is further decorated with hemispherical Ni or Pt NPs grown by electrodeposition. Electrodeposition offers several advantages compared to chemical synthesis: in addition to guaranteeing a good electrical contact between the NPs and the substrate,[34] it can produce NPs with a wide range of sizes, allowing for the screening of size-dependent electrochemistry at the single NP level.[35,36] Moreover, optical microscopy allows an *in situ* monitoring of the NPs' growth.[37–39]

The surface confined by a miniaturized electrochemical cell containing a Ni^{2+} solution is subjected to HER by applying a negative potential bias cycle in a cyclic voltammetry (CV) experiment (Figure 1c) while optical images of the surface are continuously acquired under optical microscopy observation in a reflection mode at 20 Hz by a CMOS camera.

Figure 1b shows the optical image corresponding to an individual 145 nm radius hemispherical Pt NP electrodeposited on an ITO electrode. Details about the Pt NPs electrodeposition procedure, the CV response for the HER and the NPs *ex situ* characterization are provided in SI sections 0 and 2 SI1, SI2 and SI3 respectively. The Pt NP is detected as a bright central disk surrounded by a small dark halo. Such interference pattern is common for this interferometric optical detection mode. As evidenced in the lower panels of Figure 1b and c, upon polarizing the ITO negatively, the dark halo grows in size around the NP. The halo, or NP, is characterized by its apparent outer radius r_{halo} whose dynamic growth is monitored (lower panel of Figure 1c; details about the r_{halo} estimate from the optical images are given in SI section SI1). The halo grows within a restricted negative bias range such that E < -1.2 V vs Pt (region denominated HER in the upper panel of Figure 1c). Such potential bias suggests that the halo's formation originates from the Pt NP catalyzing water reduction and producing HO^- ions (3), triggering the precipitation of the Ni^{2+} ions present in solution in the form of insoluble $Ni(OH)_2$.

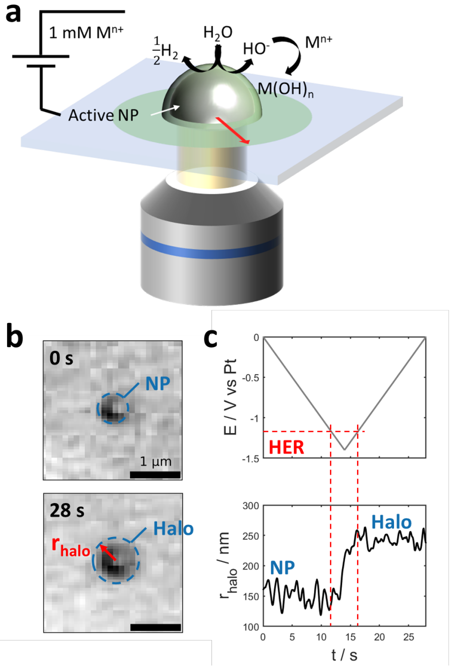

Figure 1. **a** Scheme of the strategy for evaluating the water reduction rate at single active NPs immobilized on an ITO electrode from the local precipitation of a thin metal hydroxide layer. **b** Optical images (blue channel) of a single Pt NP at the beginning (top) and at the end (bottom) of the potential cycle presented in **c** showing the growth of a dark halo around the NP. The experiment is performed in 1 mM $NiCl_2$ + 10 mM KCl solution at a scan rate of 50 mV/s. **c** Potential cycle applied at the ITO (top, current response in SI Section SI2) and corresponding evolution of halo's radius r_{halo} (defined in **b**, bottom) as a function of time. The vertical red dashed lines delineate the time domain of r_{halo} evolution, highlighting the potential domain where water reduction (HER) proceeds at detectable rates for this footprinting strategy.

SEM and TEM were used to perform EDX analyses and nanoscale chemical mappings (see SI sections SI3.3 and SI3.4) on individual Pt NPs after the HER reaction. They showed that the Pt NPs are covered by a shell made mostly of an amorphous layer containing Ni and O as is the halo formed around the NP, on the electrode. Still, a few crystallites were spotted at the edge of the NPs. However, these were poorly crystallized, and their crystal structure could not be identified (Figure SI3.4c). These results are consistent with literature suggesting that electrochemical conditions favor the electroprecipitation of amorphous $Ni(OH)_2$.[42] It indicates that along the HER the Pt NP is transformed into a core-shell $Pt@Ni(OH)_2$ NP surrounded by a halo of $Ni(OH)_2$.

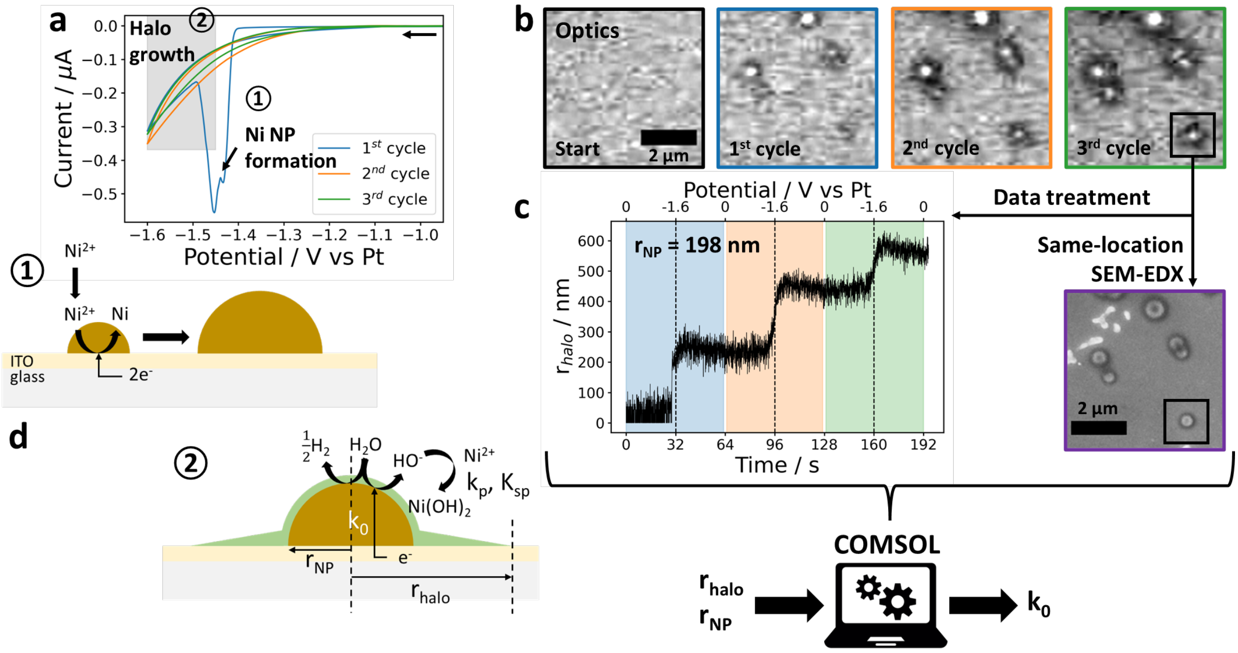

Figure 2. **a** CV within a ca. 100 µm droplet of 1 mM $NiCl_2$ + 0.1 M KCl solution on ITO (scan rate: 50 mV/s). **b** Series of optical images acquired (from left to right) at the beginning of the experiment and at the end of each CV cycle (at 0 V) showing the growth of Ni NPs (bright features) followed by the growth of a dark halo around them. **c** Evolution of r_{halo} for the NP framed in b during the whole experiment, correlated SEM image acquired *ex situ* at the end of the experiment, and schematic representation of the processing of r_{halo} and r_{NP} to determine k_0. **d** Schemes of the proposed mechanism for the formation of Ni NPs ① followed by the formation of $Ni(OH)_2$ halos around them ②.

Next, the presence of this halo as a chemical footprint of the HER, is tested for different NP chemistries and M^{2+} cations then it is used to quantify the catalytic activity of single NPs.

The same behavior is also observed with Ni NPs (Figure 2). In this case, both the Ni NP electrodeposition and their HER activity are probed during the same CV experiment by sweeping the potential negatively from 0 to -1.6 V vs Pt along three successive cycles. As shown in Figure 2a and b, during the first cycle a characteristic peak of Ni electrodeposition appears at ca. -1.45 V concomitantly to bright-contrasted features on the surface.[40,41] From previous studies, these optical features are related to the growth of hemispherical metallic Ni NPs from the electrode surface.[25,39]

As for the Pt NP presented in Figure 1, at more negative potentials and during the subsequent backward scan (as well as during the subsequent cycles), a dark halo is detected optically, gradually growing, around all Ni NPs (Figure 2b). The evolution of r_{halo} over the three cycles for an average-sized and well-isolated Ni NP (black frame in Figure 2b) is reported in Figure 2c. The halo is clearly increasing in size during the subsequent cycles and in all cases for electrode potentials more negative than -1.45 V. The halo is therefore mostly produced and growing concomitantly to the water reduction.

Same-location optical, SEM and AFM analyses were performed at the end of the first potential sweep on another sample (see SI, section SI4). As already visible in Figure 2c, a dark halo is also detected around the Ni NPs on the SEM images. Comparing the optical and SEM profiles of a Ni NP in Figure SI4.1 shows that the dark-contrasted regions (in grey) are of the same size, ca. 370 nm in that case. At that distance, the thickness of the halo measured by AFM is ca. 5 nm, demonstrating that it corresponds to a thin layer of deposited material and not to an imaging artifact. It also gives an estimate of the detection limit of our optical microscope (see below).

The mechanism explaining the formation of the amorphous layer of $Ni(OH)_2$, and the growth of the optically detected halo, is schematized in Figure 2d. As for the Pt NP shown in Figure 1c, the halo's growth is observed while the CV shows an exponential current decrease due to water reduction on the freshly electrodeposited Ni NPs (Figure 2a). The HO^- ions produced by this reaction (3) likely combine with Ni^{2+} ions from the solution to form the amorphous $Ni(OH)_2$ shell around the NPs ($Ni(OH)_2$ has a very low solubility product, see section SI5, Table SI5-1). Hence, the radius of the halo, r_{halo}, is indicative of the extent of local HO^- liberation during the electrocatalytic reaction proceeding at the individual NP. As a chemical footprint, the halo then reveals the dynamics of local HO^- production by the NP and therefore provides an independent measure of its catalytic activity towards water reduction. Noteworthy, oxygen reduction is another electrochemical reaction generating HO^- ions. The contribution of oxygen reduction is clearly detected in the CV response at the Pt decorated electrode starting from -0.8 V vs Pt (Figure SI2). However, the halo's growth is only detected at more negative potential, ca. -1.2 V (see Figure 1c), when more cathodic current assigned to water reduction is flowing. It suggests that oxygen reduction is not sufficient by itself to initiate or propagate the precipitation of $Ni(OH)_2$ at this scan rate.

As evidenced in Figure 2c, r_{halo} expands inequivalently during each electrode potential cycle, hinting at changes in the HER kinetics and its dependence on the NP structure which is evolving along the successive potential cycles. To quantify these changes, we propose a COMSOL model which explicitly simulates the precipitation of $Ni(OH)_2$ on top of an electrocatalytically active NP.[43] Details about the model can be found in the SI, section SI5. The model essentially depends upon four parameters: the electron transfer rate constant associated to water reduction on the NP (k_0) dictating the rate of HO^- production from the NP, the solubility product of $Ni(OH)_2$ (K_{sp}), the precipitation rate constant of $Ni(OH)_2$ (k_p), and the optical limit of detection of the $Ni(OH)_2$ layer (lod). However, the results were found to depend very little on the lod (see Table SI5-2), which was fixed at 5 nm according to same-location SEM and AFM measurements (see Figure SI4.1 and above). From a simplified version of the model (detailed in SI section 1), an analytical expression of the transient evolution of the halo's radius can be proposed showing that it depends on a single parameter, the product $k_0^2 k_p$. This interdependency of $k_0$and k_p is confirmed from the simulations discussed in Figure SI1-3. It then suggests that to determine the absolute value of the water reduction rate constant, k_0, the knowledge of the precipitation rate constant, k_p, of the metal hydroxide is required.

Rather than for precipitation kinetics, databases are available for the reverse reaction i.e., crystal dissolution.[44] These are usually obtained by titration of the solution during a dissolution reaction. Herein, the dissolution rate of the metal hydroxide thin film halo can also be evaluated optically from the slow dynamics of decrease in r_{halo} when the halo thin film is in contact with water. Since no electrochemical reaction is involved in this process, the decrease in r_{halo} during dissolution reaction now only depends upon k_p, making it possible to determine the absolute value of this parameter. A detailed discussion of these experiments can be found in the SI, section SI5. From such analysis, the rate constant for $Ni(OH)_2$ precipitation is found: $k_{p,Ni(OH)_2} = 5.1\,10^{-4}\,m^7\,mol^{-2}\,s^{-1}$. This corresponds to a dissolution rate constant of $2.8\,10^{-14}\,mol\,cm^{-2}\,s^{-1}$, which is close to the value reported in the literature for NiO.[44]

The knowledge of this precipitation rate constant allows the analysis of the electrochemical growth of the $Ni(OH)_2$ halo upon water reduction. The results of the simulation reproducing the experiment in Figure 2 of the electrochemical growth of a $Ni(OH)_2$ layer around a Ni NP upon water reduction are presented in Figure 3 and Table SI5-6. The simulation consists in matching the transient evolution of the halo's size, r_{halo}, during the three cycles of the CV experiment, as depicted in Figure 3a. The simulation takes into account the electrogeneration of HO^- ions at the NP surface and its later precipitation with cations present in solution. This precipitation is described here, as seen in Figure 3b, through the formation of a new phase atop and around the NP. Noteworthy, the concentration profiles of the species are provided in Figure SI5-1. Such experiment is first analyzed along the first cycle of the CV. From the knowledge of $k_{p,Ni(OH)_2}$, the observed halo size matching with the simulation (Figure 3a orange and black lines) yields a water reduction rate constant k_0 of $1.3\,10^{-7}\,cm\,s^{-1}$. It is of the same order of magnitude as the value determined by microscale local electrochemical probing (considering that the activity of water is equal to $1\,mol\,L^{-1}$),[45] indicating no significant differences between micro- and nanoscale in agreement with Compton *et al.*.[18] At this stage, it is worth mentioning that in potential region ② (Figure 2a,d), the catalytic activity of a core-shell $Ni@Ni(OH)_2$ is more likely probed, the Ni core being already covered with a thin layer of $Ni(OH)_2$ produced during the electrodeposition of Ni and naturally forming on bare Ni when exposed to water. In water, the catalytic activity of bare Ni can only be probed at the earliest stage of Ni nucleation i.e., during the characteristic reduction peak mentioned above. During this narrow time window, the catalytic activity was recently shown to be two orders of magnitude higher than what is reported in the literature.[25,45]

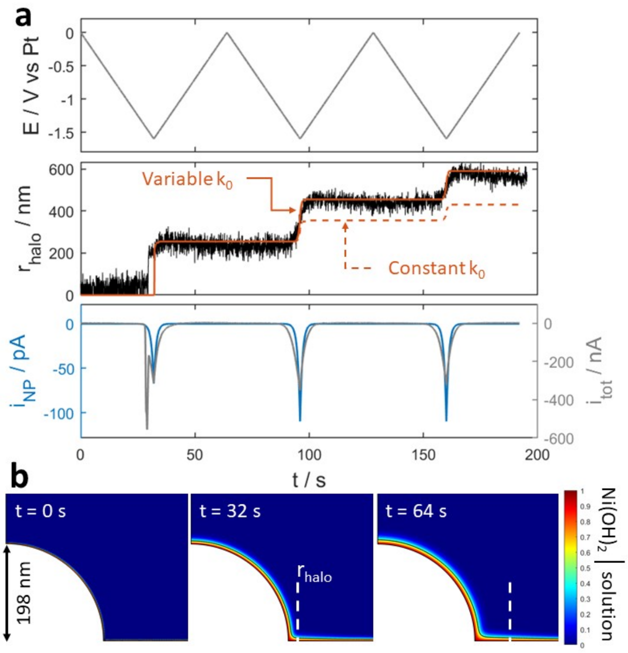

Figure 3. a Simulation of the evolution of r_{halo} for the NP framed in Figure 2b and c for a constant value of k_0 ($1.3\,10^{-7}\,cm\,s^{-1}$, dashed orange line) and for a variable value of k_0 (respectively $1.3\,10^{-7}$, $2.0\,10^{-7}$ and $2.0\,10^{-7}\,cm\,s^{-1}$, solid orange line; $k_p = 5.1\,10^{-4}\,m^7\,mol^{-2}\,s^{-1}$, lod = 5 nm). The blue line in the lower panel represents the simulated current which flows through the NP in the case of a variable value of k_0 (solid orange line) and the grey line represents the experimental current flowing through the entire electrode. b Screenshots of the simulated $Ni(OH)_2$ deposit at different times during the first CV cycle; the white vertical dashed line shows how r_{halo} is determined assuming a deposit of thickness 5 nm.

Next, the two subsequent cycles are simulated. When the same value of k_0 is used for all three cycles, the simulation does not fit the experimental transient (dashed orange line in Figure 3a). As mentioned above, it is not a question of lod as, from the simulation, the ratio between plateaus remains approximately the same for lod = 1, 5, and 10 nm (Table SI5-3). It could be due to the delay introduced by the fact that the NPs nucleate after the onset of water reduction during the first cycle, but the charge corresponding to this delay is negligible (Figure SI5-4). This means that the rate of water reduction increases from cycle to cycle (solid orange line in Figure 3a). It indicates that increasing the thickness of the $Ni(OH)_2$ shell increases the water reduction rate at Ni-based NPs. This evolution of k_0 agrees with previous reports stating that the presence of $Ni(OH)_2$ enhances the catalytic activity of Ni.[5]

The simulation further enables estimating the current for water reduction at the single NP level. The simulated single NP water reduction current is provided Figure 3a (lower panel, blue curve) along the three cycles. It tracks nicely (except for the Ni electrodeposition peak) the overall experimental current recorded for the whole electrode region. It suggests that all electrodeposited NPs might behave similarly. It also shows that the footprinting strategy provides a means to image electrocatalytic reactions at considerably low current: for the 198 nm radius NP considered in Figure 3a, a HER current of the order of 10 pA could be evaluated, indirectly from such footprint strategy. This corresponds to much lower current density (about 3 orders of magnitude) than that required to initiate the formation of a H_2 nanobubble. The footprinting strategy then allows expanding the scope of quantitative optical imaging to a wider range of reaction kinetics.

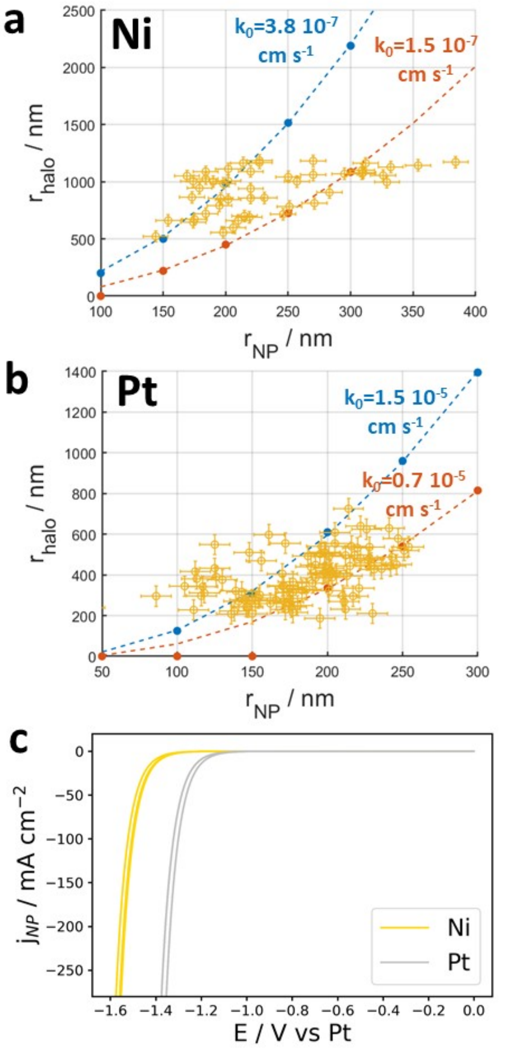

Figure 4. Influence of NP size and composition on water reduction activity in the presence of Ni^{2+}; evaluated from the fit of the experimental r_{halo} for all NPs after the 3rd cycle. **a**, **b**. Size effect analyzed through a bimodal behavior of low (orange) and high (blue) k_0 values of activity evaluated for two characteristic NP sizes (see text); **a** for Ni NPs, the smallest (most active) population is described by NP1 of radius $r_{NP1} = 184\,nm$ while the largest (less active) population is described by NP5 ($r_{NP5} = 271\,nm$); **b** Same with Pt NPs ($r_{NP1} = 171\,nm$ and $r_{NP5} = 243\,nm$). **c** Reconstructed CVs of Ni and Pt NPs of same radius (respectively $r_{NP} = 206\,nm$ and $r_{NP} = 203\,nm$).

NPs of various sizes are then analyzed in Figure 4a in order to discuss size effect in terms of initial activity, activation or passivation. The simulation allows to predict the evolution of the activity as a function the NP size: a parabolic law ($k_0 \sim r_{NP}^2$) is expected, as illustrated by the simulated orange and blue lines in Figure 4a for two typical k_0 values. Experimentally, the halo radius is estimated from the optical image, while the NP size (or its radius in Figure 4) is evaluated from identical-location SEM images (examples are given in section S3 and S4 of the SI). The distribution of NPs sizes was clustered in five sub-groups characterized by a characteristic median NP size (NP_1 to NP_5).

The values of k_0 for these five characteristic NPs were then evaluated from the fit of the experimental evolution of the halo growth. The characteristic NPs of the smallest and the largest sub-groups, with respective size $r_{NP1} = 184\,nm$ and $r_{NP5} = 271\,nm$, are actually simulated by two different representative k_0 values: the smallest, and most active, NP_1 corresponds to the orange line in Figure 4a, while the largest, and less active, NP_5 corresponds to the blue line in Figure 4a. The experimental halos of the whole set of NPs, with size spanning from ca. 145 to 380 nm, is then compared to those two representative activities in Figure 4a. It shows that smaller NPs ($r_{NP} < 200\,nm$) follow the trend of the most active (and smallest) NP_1, whereas larger NPs ($r_{NP} > 200\,nm$) follow the trend of the less active (and largest) NP_5. Similar analysis made over the three cycles (Figure SI5-5) also show that the largest NPs even tend to passivate after the second cycle.

It is interesting to note that NPs of similar r_{NP} can produce significantly different r_{halo}. Indeed, the error on the determination of r_{halo} (ca. 50 nm or 1 px) alone cannot explain the dispersity observed in Figure 4a,b. This suggests that r_{NP} is not the only parameter influencing the electrocatalytic activity, but maybe also the crystal structure which cannot be probed neither by *in situ* optical microscopy nor *ex situ* identical-location SEM.[46] This error on the determination of r_{halo} translates into a ca. 20% error on the determination of k_0.

The methodology is highly versatile as proved by the first experiment (summarized in Figure 1) in which electrodeposited Pt NPs similarly subjected to water reduction in the presence of Ni^{2+} ions, yield the growth of $Ni(OH)_2$ halo around the NPs. Since water reduction occurred earlier than the nucleation potential of Ni (> -1.4 V), the Pt NPs can be considered as more active than the Ni@$Ni(OH)_2$ NPs. This is confirmed from the values of k_0 determined from the simulated CVs given in Figure 4c and halo imaged in Figure SI3.2-1. Starting from k_0 values $\approx 10^{-6}\ cm\ s^{-1}$ for the pristine Pt NPs, in agreement with literature,[47] an enhancement of activity is observed along consecutive cycles, when electrocatalysis at Pt@$Ni(OH)_2$ is rather probed. It indicates a synergistic effect of $Ni(OH)_2$ shell on the water reduction electrocatalysis in neutral media. Finally, the influence of Pt NP size on activity was also studied (Table SI5-7 and Figure 4b). As seen in Figure 4b, the activity of Pt@$Ni(OH)_2$ NPs could also be clustered between two groups of more active and less active NPs depending on their size.

To further test the versatility of our method in terms of footprint chemistry, the same Pt NPs (on another spot of the same ITO substrate) were then subjected to water reduction this time in the presence of Mg^{2+} ions. The latter have the advantage of preventing unwanted side reactions such as electrodeposition and have not been shown to have a significant effect on water reduction kinetics in dissolved form.[48] In this case as well, a dark halo is detected around the Pt NPs on the optical images (Figure SI3.2-2). The halo is then very likely composed of $Mg(OH)_2$ as suggested by a SEM-EDX mapping of the resulting structures (Figure SI3.3-3). Even though the absolute values of k_0 determined for Pt NPs using both Mg and Ni precipitates are different, their evolution can be compared. The relative activity of Ni and Pt NPs (covered in both $Ni(OH)_2$ and $Mg(OH)_2$) along the three CV cycles is shown in Figure 5 in the form of a histogram. From this plot, one can conclude that $Ni(OH)_2$ enhances the catalytic activity of Ni and Pt NPs, whereas $Mg(OH)_2$ only blocks the activity of the Pt NPs. This clearly demonstrates the bifunctional effect of $Ni(OH)_2$ and Ni/Pt.

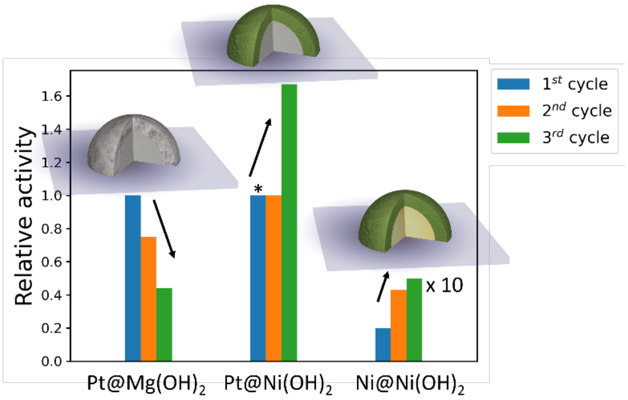

Figure 5. Histogram of the relative activity for water reduction electrocatalysis for NPs of comparable sizes along the three CV cycles for each composition. For Pt, the relative activity corresponds to the activity at cycle *i* compared to that at first cycle, $\frac{k_{0,i}}{k_{0,1}}$, evaluated for Pt NP of $r_{NP} = 154\ nm$ and $r_{NP} = 145\ nm$. For Ni NPs, the activity along cycles is compared to that of Pt NP, $\frac{k_{0,i}}{k_{0,1}(Pt@Ni(OH)_2)}$, and is evaluated for a Ni NP with $r_{NP} = 184\ nm$. *The relative activity is assumed to be the same between the first and the second cycle because r_{halo} lies close to the detection limit during the first cycle (see Table SI5-7).

Conclusion

In conclusion, we have demonstrated that the catalytic activity towards water reduction of single NPs can be measured by optically monitoring the growth of insoluble hydroxide halos forming around the NPs, which are used as footprints of the electrocatalytic reaction. A COMSOL model was proposed to quantify the electron transfer rate constant associated to water reduction at individual NPs from the dynamics of the footprint. Experiments showed that Ni and Pt NPs become more active after the first and the second cycle when $Ni(OH)_2$ is used as nano-shell, whereas they become less active when $Mg(OH)_2$ is used instead. This is consistent with previous reports stating that $Ni(OH)_2$ specifically enhances the catalytic activity of Ni and Pt via a bifunctional effect, while $Mg(OH)_2$ only blocks the NPs. The optical monitoring also revealed that larger NPs ($r_{NP} > 200\ nm$) are less active and activate less than smaller ones ($r_{NP} < 200\ nm$).

In addition to confirming the bifunctional effect of Ni/Pt and $Ni(OH)_2$ on water reduction activity for single NPs with ≈ 50 nm limit of detection (for the halo to be detected), the present study provides a powerful method for the measurement and screening of the activity of single NPs towards reactions involving the production of HO^- ions and not necessarily of gas nanobubbles, like nitrate or CO_2 reduction for example. But more importantly than providing a means to image reactions which do not produce gases, this method allows to probe electrocatalysts at much lower – industrially-relevant – current densities than methods using gas nanobubbles as a proxy.

Furthermore, this strategy is not limited to optical microscopy but could also readily be applied to other types of *in situ* probing such as electron microscopies. We hope that this study will pave the way for a more efficient measurement of the intrinsic catalytic activity of single NPs which would help screening structure-activity relationships of new bifunctional catalysts.

Supporting Information

The authors have cited additional references within the Supporting Information.[49-52]

Data Availability Statement

The data that support the findings of this study are openly available in the "Zenodo" public repository at http://doi.org/10.5281/zenodo.7948233, reference number 7948233. The data are explained in the Supporting Information of this article.

Acknowledgements

P.C. and F.K. acknowledge funding from the European Union's Horizon 2020 research and innovation program under the Marie Skłodowska-Curie MSCA-ITN grant agreement no. 812398, through the single entity nanoelectrochemistry, SENTINEL, project. We thank the "Emergence Ville de Paris" program and the ANR through the Labex SEAM (Science and Engineering for Advanced Materials and devices, ANR-10-LABX-0096) and the JCJC program (PIRaNa project, ANR-20-CE42-0001) for their financial support to this work.

Keywords: Single entity electrochemistry • synergistic effects • hydrogen evolution reaction • operando optical microscopy • metal hydroxides

[1] K. Sun, X. Wu, Z. Zhuang, L. Liu, J. Fang, L. Zeng, J. Ma, S. Liu, J. Li, R. Dai, X. Tan, K. Yu, D. Liu, W.-C. Cheong, A. Huang, Y. Liu, Y. Pan, H. Xiao, C. Chen, *Nat. Commun.* **2022**, *13*, 6260.

[2] W. Tong, M. Forster, F. Dionigi, S. Dresp, R. Sadeghi Erami, P. Strasser, A. J. Cowan, P. Farràs, *Nat. Energy* **2020**, *5*, 367–377.

[3] J. Guo, Y. Zhang, A. Zavabeti, K. Chen, Y. Guo, G. Hu, X. Fan, G. K. Li, *Nat. Commun.* **2022**, *13*, 5046.

[4] J. Durst, A. Siebel, C. Simon, F. Hasché, J. Herranz, H. A. Gasteiger, *Energy Environ. Sci.* **2014**, *7*, 2255–2260.

[5] R. Subbaraman, D. Tripkovic, D. Strmcnik, K. C. Chang, M. Uchimura, A. P. Paulikas, V. Stamenkovic, N. M. Markovic, *Science* **2011**, *334*, 1256–1260.

[6] Q. Liu, Q. Liu, Z. Yan, J. Gao, J. Gao, E. Wang, G. Sun, *ACS Appl. Mater. Interf.* **2020**, *12*, 24683–24692.

[7] L. Wang, C. Lin, D. Huang, J. Chen, L. Jiang, M. Wang, L. Chi, L. Shi, J. Jin, *ACS Catal.* **2015**, *5*, 3801–3806.

[8] R. Kavian, S. il Choi, J. Park, T. Liu, H. C. Peng, N. Lu, J. Wang, M. J. Kim, Y. Xia, S. W. Lee, *J. Mater. Chem. A* **2016**, *4*, 12392–12397.

[9] H. Yin, S. Zhao, K. Zhao, A. Muqsit, H. Tang, L. Chang, H. Zhao, Y. Gao, Z. Tang, *Nat. Commun.* **2015**, *6*, 6430.

[10] L. Wang, Y. Zhu, Z. Zeng, C. Lin, M. Giroux, L. Jiang, Y. Han, J. Greeley, C. Wang, J. Jin, *Nano Energy* **2017**, *31*, 456–461.

[11] G. Yuan, B. Wen, Y. Hu, G. Zeng, W. Zhang, L. Wang, X. Zhang, Q. Wang, *Int. J. Hydrogen Energy* **2019**, *44*, 14258–14265.

[12] N. Danilovic, R. Subbaraman, D. Strmcnik, K. C. Chang, A. P. Paulikas, V. R. Stamenkovic, N. M. Markovic, *Angew. Chem. Int. Ed.* **2012**, *51*, 12495–12498.

[13] R. Subbaraman, D. Tripkovic, K. C. Chang, D. Strmcnik, A. P. Paulikas, P. Hirunsit, M. Chan, J. Greeley, V. Stamenkovic, N. M. Markovic, *Nat. Mater.* **2012**, *11*, 550–557.

[14] Z. Zeng, K. C. Chang, J. Kubal, N. M. Markovic, J. Greeley, *Nat. Energy* **2017**, *2*, 17070.

[15] F. J. Sarabia, P. Sebastián-Pascual, M. T. M. Koper, V. Climent, J. M. Feliu, *ACS Appl. Mater. Interf.* **2019**, *11*, 613–623.

[16] M. Gong, W. Zhou, M. C. Tsai, J. Zhou, M. Guan, M. C. Lin, B. Zhang, Y. Hu, D. Y. Wang, J. Yang, S. J. Pennycook, B. J. Hwang, H. Dai, *Nat. Commun.* **2014**, *5*, 4695.

[17] A. R. Akbashev, *ACS Catal.* **2022**, *12*, 4296–4301.

[18] Y. G. Zhou, N. v. Rees, R. G. Compton, *Phys. Chem. Chem. Phys.* **2013**, *15*, 761–763.

[19] J. Kim, C. Renault, N. Nioradze, N. Arroyo-Currás, K. C. Leonard, A. J. Bard, *J. Am. Chem. Soc.* **2016**, *138*, 8560–8568.

[20] T. Sun, H. Zhang, X. Wang, J. Liu, C. Xiao, S. U. Nanayakkara, J. L. Blackburn, M. v. Mirkin, E. M. Miller, *Nanoscale Horiz.* **2019**, *4*, 619–624.

[21] T. Sun, Y. Yu, B. J. Zacher, M. V. Mirkin, *Angew. Chem. Int. Ed.* **2014**, *53*, 14120–14123.

[22] J.-G. Wang, L. Zhang, J. Xie, Y. Weizmann, D. Li, J. Li, *Nano Lett.* **2022**, *22*, 5495-5502.

[23] X. Shan, I. Díez-Pérez, L. Wang, P. Wiktor, Y. Gu, L. Zhang, W. Wang, J. Lu, S. Wang, Q. Gong, J. Li, N. Tao, *Nat. Nanotechnol.* **2012**, *7*, 668–672.

[24] J.-F. Lemineur, P. Ciocci, J.-M. Noël, H. Ge, C. Combellas, F. Kanoufi, *ACS Nano* **2021**, *15*, 2643–2653.

[25] L. Godeffroy, J.-F. Lemineur, V. Shkirskiy, M. Miranda Vieira, J.-M. Noël, F. Kanoufi, *Small Methods* **2022**, *6*, 2200659.

[26] R. Hao, Y. Fan, M. D. Howard, J. C. Vaughan, B. Zhang, *Proc. Natl. Acad. Sci. U S A* **2018**, *115*, 5878–6588.

[27] R. Hao, Y. Fan, T. J. Anderson, B. Zhang, *Anal. Chem.* **2020**, *92*, 3682–3688.

[28] Q. Chen, L. Luo, H. Faraji, S. W. Feldberg, H. S. White, *J. Phys. Chem. Lett.* **2014**, *5*, 3539–3544.

[29] A. Steinegger, O. S. Wolfbeis, S. M. Borisov, *Chem. Rev.* **2020**, *120*, 12357–12489.

[30] M. C. O. Monteiro, M. T. M. Koper, *Curr. Opin. Electrochem.* **2021**, *25*, 100649.

[31] N. C. Rudd, S. Cannan, E. Bitziou, I. Ciani, A. L. Whitworth, P. R. Unwin, *Anal. Chem.* **2005**, *77*, 6205–6217.

[32] M. Saqib, Y. Fan, R. Hao, B. Zhang, *Nano Energy* **2021**, *90*, 106539.

[33] H. Xin, H. Wang, W. Zhang, Y. Chen, Q. Ji, G. Zhang, H. Liu, A. D. Taylor, J. Qu, *Angew. Chem. Int. Ed.* **2022**, *61*, e202206236.

[34] W. Wei, T. Yuan, W. Jiang, J. Gao, H. Y. Chen, W. Wang, *J. Am. Chem. Soc.* **2020**, *142*, 14307–14313.

[35] J.-F. Lemineur, J.-M. Noël, D. Ausserré, C. Combellas, F. Kanoufi, *Angew. Chem. Int. Ed.* **2018**, *130*, 12174–12178.

[36] M. Bernal Lopez, J. Ustarroz, *Curr. Opin. Electrochem.* **2021**, *27*, 100688.

[37] L. Godeffroy, P. Ciocci, J.-F. Lemineur, F. Kanoufi, *Curr. Opin. Electrochem.* **2022**, *36*, 101165.

[38] P. Ciocci, D. Valavanis, G. N. Meloni, J.-F. Lemineur, P. R. Unwin, F. Kanoufi, *ChemElectroChem* **2023**, *10*, e202201162.

[39] L. Godeffroy, P. Ciocci, A. Nsabimana, M. Miranda Vieira, J.-M. Noël, C. Combellas, J.-F. Lemineur, F. Kanoufi, *Angew. Chem. Int. Ed.* **2021**, *60*, 16980–16983.

[40] N. L. Ritzert, T. P. Moffat, *J. Phys. Chem. C* **2016**, *120*, 27478–27489.

[41] R. Wang, U. Bertocci, H. Tan, L. A. Bendersky, T. P. Moffat, *J.Phys. Chem. C* **2016**, *120*, 16228–16237.

[42] H. B. Li, M. H. Yu, F. X. Wang, P. Liu, Y. Liang, J. Xiao, C. X. Wang, Y. X. Tong, G. W. Yang, *Nat. Commun.* **2013**, *4*, 1894.

[43] W. Sun, G. Liu, L. Wang, T. Wu, Y. Liu, *J. Solid State Electrochem.* **2013**, *17*, 829–840.

[44] J. Wang, *J. Mater. Res.* **2020**, *35*, 898–921.

[45] Z. Liang, H. S. Ahn, A. J. Bard, *J. Am. Chem. Soc.* **2017**, *139*, 4854–4858.

[46] Q. Wei, P. Wang, Y. Ma, K. Du, H. Yin, H. Zhu, D. Wang, *J. Electroanal. Chem.* **2022**, *923*, 116833.

[47] P. J. Rheinländer, J. Herranz, J. Durst, H. A. Gasteiger, *J. Electrochem. Soc.* **2014**, *161*, F1448–F1457.

[48] M. C. O. Monteiro, F. Dattila, N. López, M. T. M. Koper, *J. Am. Chem. Soc.* **2022**, *144*, 1589–1602.

[49] V. Shkirskiy, L. C. Yule, E. Daviddi, C. L. Bentley, J. Aarons, G. West, P. R. Unwin, *J. Electrochem. Soc.* **2020**, *167*, 041507.

[50] COMSOL. “Under-Deposit Corrosion”. https://www.comsol.com/model/under-deposit-corrosion-67821

[51] H. Sato, M. Yui, H. Yoshikawa, *J. Nucl. Sci. Technol.* **1996**, *33*, 950–955.

[52] W.M. Haynes, D.R. Lide, T.J. Bruno, in *CRC Handbook of Chemistry and Physics. Vol. 268*, CRC Press, **2016**.

[53] D. Hanselman, “Contour Plot for Scattered Data MATLAB Central File Exchange.” Retrieved August 25, **2021**. https://www.mathworks.com/matlabcentral/fileexchange/38858-contour-plot-for-scattered-data